Cryogenic optical shadow sensors for gravitational wave detectors

Ubhi, Amit Singh; Bryant, John; Hoyland, David; Martynov, Denis

Document Version
Publisher's PDF, also known as Version of record

Cryogenic optical shadow sensors for gravitational wave detectors

Amit Singh Ubhi, John Bryant, David Hoyland, Denis Martynov

Institute for Gravitational Wave Astronomy, School of Physics and Astronomy, University of Birmingham, Birmingham B15 2TT, United Kingdom

ABSTRACT

Displacement sensors have a variety of applications within gravitational wave detectors. The seismic isolation chain of the LIGO core optics utilises optical shadow sensors for their stabilisation. Future upgrades, such as LIGO Voyager, plan to operate at cryogenic temperatures to reduce their thermal noise and will require cryogenic displacement sensors. We present the results of simulations and experimental tests of the shadow sensors embedded in the Birmingham Optical Sensors and Electromagnetic Motors (BOSEMs) to establish whether BOSEMs are suitable candidates for cryogenic applications. We determine that the devices can reliably operate at 100 K, and an improvement in their performance is seen due to the improved quantum efficiency of the LED by a factor of 2.7. The shot noise improvement due to the electronic changes of the readout's amplifier (satellite amplifier) results in a shot noise enhancement from $6 \times 10^{-11} \mathrm{m}/\sqrt{\mathrm{Hz}}$ at room temperature, to $4.5 \times 10^{-11} \mathrm{m}/\sqrt{\mathrm{Hz}}$ under cryogenic conditions.

1. Introduction

Terrestrial gravitational wave detectors such as Advanced LIGO [1] have detected a number of gravitational wave sources since 2015 [2–4], varying from compact binary sources such as binary black hole mergers [5–7], binary neutron star inspirals [8], and potential black hole neutron star mergers [9]. Within their most sensitive band, the aLIGO detectors are limited by quantum shot noise and thermal noises of the main optics [10,11]. To combat the thermal noise, the KAGRA [12,13] detector cools its core optics. Future upgrades and detectors such as LIGO Voyager [14], the Einstein Telescope [15], and Cosmic Explorer [16,17] also plan to operate at cryogenic temperatures to reduce their thermal noise [18,19]. In the case of LIGO Voyager, the core optics will have a silicon substrate. The material exhibits good mechanical properties at cryogenic temperatures and also has a negligible thermal expansion coefficient at 123 K [14].

Similar to the current gravitational wave detectors, future observatories will require a comparable or even more sophisticated seismic isolation system [20–22]. The design of the isolation systems is different in LIGO, Virgo, and KAGRA. However, the detectors share the same isolation principle: suspend the test masses using a multi-stage pendulum suspension to passively filter ground vibrations above the suspension resonances. The resonances of each stage are actively damped using Optical Sensors and Electromagnetic Motors (OSEMs) [23,24]. The same devices monitor the position of the suspension chain using an optical shadow sensor scheme encased within the device. The Birmingham design of OSEMs (BOSEMs), and another design known as Advanced LIGO OSEMs have proven their reliability, large linear range, and ultra high vacuum compatibility at the LIGO observatories. We believe BOSEMs would be a perfect candidate as an auxiliary sensor for next generation observatories if they can be shown to be operational at cryogenic temperatures.

In this paper, we study the cool down and operation of the BOSEM, focusing on the sensing scheme, via simulation and experimental methods to determine whether the sensor is reliable at cryogenic temperatures. We discuss the potential concerns of cooling the device, and simulate the cool down and stresses involved for the readout components using finite element analysis.

Experimental tests at cryogenic temperatures were conducted to determine if future design considerations were required, and to compare with the simulation results. Measurements of the device's noise were conducted, and its characteristics analysed to understand the discrepancies between room temperature and cryogenic operation.

2. Finite-element analysis

Initially, we simulated the cool down procedure of our experimental setup. The setup consists of two main parts: a thermal restrictor and a BOSEM. The restrictor was machined from aluminium and connects the BOSEM to a liquid nitrogen reservoir. The restrictor design was

optimised for temperature tuning of the BOSEM with two power resistors located on the restrictor plate as shown in Fig. 1. The figure also shows an exploded view of the BOSEM. The shadow sensing is achieved by an LED and a photodetector (PD): a measured target blocks part of the LED light to change the PD signal [25]. Both the LED and PD are embedded in the separate assemblies consisting of cylindrical parts for stability and electrical insulation.

The photodetector and LED assemblies are the main concerns during the cool down process because the elements are manufactured from materials with different indices of thermal expansion. Therefore, temperature gradients during the cool down process and uneven contraction of the assembly elements can cause stresses in the device. In particular, the LED and photodetector sleeves are made of MACOR for their electrical insulation while their carriers are made of aluminium to simplify the production process. During cool down, the aluminium carriers would contract more than MACOR, applying a compressive load on the sleeves which may potentially lead to fractures or failure of the component. However, the tolerances of the components allow for the slight excess movement of the sleeve within the carrier. At room temperature, the carrier's inner diameter is, $d_{\text{carrier}} = 7.290^{+0.015}_{-0.000}$ mm, with the sleeve having outer diameter, $d_{\text{sleeve}} = 7.239^{+0.000}_{-0.036}$ mm. Assuming a constant coefficient of linear expansion over the temperature range during cooling, the inner diameter of the carrier is always larger than the maximum diameter of the sleeve which should result in no compressive stress.

We conducted the analyses of the cool down process with the Autodesk Inventor Nastran add-on [26]. The material parameters are shown in Table 1. The software did not allow for temperature dependency of these parameters, therefore the accuracy of the simulation was not optimal. The purpose of the study was to determine whether the stresses were excessively beyond their yield limits and where the large stresses would occur.

We achieved a transient heat transfer model with the constraint that the top of the thermal restrictor is held at 77 K. This would in practice be connected to the liquid nitrogen reservoir as highlighted in Fig. 4. For the simulation and cool down of the device, two power resistors were used for temperature control. During the simulation they were set with a constant output of 0.2 W of power, however, under experimental operation the temperature would controlled using PID feedback.

The result of the simulation was a temperature map, shown in Fig. 2. We found that the PD assembly was the component which cooled at the slowest rate which matched the experimental cool down results shown in Fig. 5.

We then utilised the results of the heat transfer simulation to calculate the stress on the system due to the temperature gradients. Fig. 3 is a cross sectional cut of the BOSEM, the highlighted section shows the stress on the MACOR sleeve within the LED carrier. We found

Table 1
A list of materials and nominal values used for the finite element analysis, where k is the thermal conductivity, and α is the coefficient of thermal expansion.

| Material	k (Wm^{-1}K^{-1})	α (K^{-1})
Aluminium	167	2.4×10^{-5}
Titanium	16.44	9×10^{-6}
PEEK	0.26	5×10^{-5}
Phosphor bronze	50	1.8×10^{-5}
Glass	1.38	7×10^{-6}
Copper	401	1.7×10^{-5}
Steel, mild	45	1.2×10^{-5}
Stainless steel	16.2	1×10^{-5}
Macor	1.46	8×10^{-6}
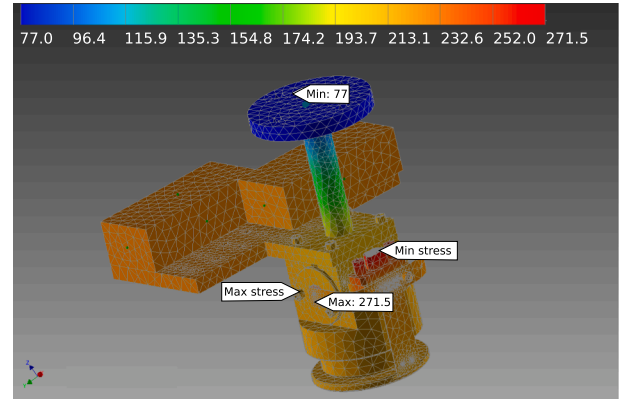
Fig. 2. Temperature (K) map of the BOSEM during the cool down simulation. This time step was chosen as it corresponded to maximum stresses in the BOSEM due to temperature variations.
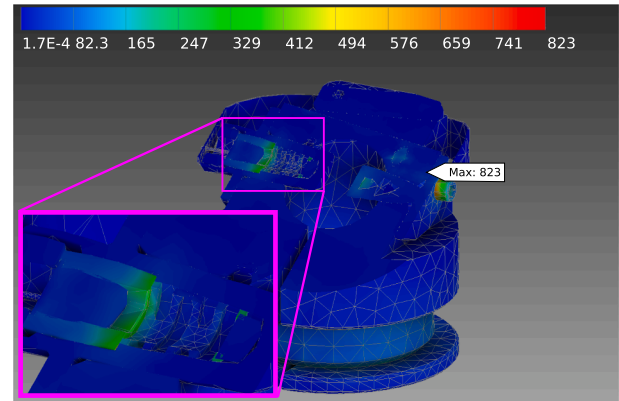
Fig. 3. Von Mises stress (MPa) map from temperature map in Fig. 2. The highlighted and zoomed section in magenta focuses on a cross section of the LED carrier and. its components.

that a significant stress comparable to its compressive breaking stress of 345 MPa occurs at the interface between the lens retainer (spring) and MACOR sleeve. However, the simulation did not allow for the initial compressive loading of the spring, and its natural length should reduce when cooled, therefore reducing the axial compressive stress applied against the sleeve. The assembly is axially compressed using the retainer nut which can not provide further compression to the assembly when cooled. This led us to believe that the components would likely survive the stresses endured during cooling. The maximum indicated stress shown in Fig. 3 occurs between a screw and the body of the BOSEM.

The constraints used in the model can not optimally characterise the stresses within the system, however they provide indication for where
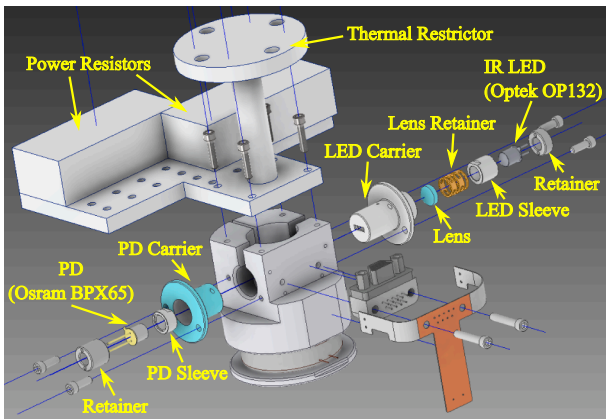
Fig. 1. Exploded view of BOSEM setup.

the areas of concern are. Experimental tests were conducted to verify the performance of the device at cryogenic temperatures.

3. Experimental results

3.1. Cool Down

Fig. 4 shows the experimental setup. The top left panel shows the BOSEM and the thermal restrictor with thermocouples attached for temperature monitoring. The top right panel shows the system wrapped in mylar to reduce the effects of radiative heating from the vacuum chamber. The bottom panel shows a schematic of the experiment and the data analysis hardware. Measurements were taken in vacuum at 2×10^{-4} mbar to reduce the thermal conductivity between the BOSEM with the environment. The nitrogen reservoir is attached to the BOSEM via the thermal restrictor. Electrical connections to the out of vacuum hardware are made via electrical feedthroughs for the temperature sensing and control using a PID controller.

We thermocycled the BOSEM more than 15 times to verify their reliability during the cool down process. The thermocouples were attached to various parts of the BOSEM and their temperatures during cooling are shown in Fig. 5. The disparity between the simulation and the BOSEM itself are likely due to the heating from the LED, and radiative heating from the vacuum chamber which were not included in the heat transfer model. During testing, the PD temperature was used in feedback, and was stabilised to a temperature of 117.7 K. A temperature below 123 K was used to ensure any discrepancy in the thermocouple reading at low temperature was accounted for, and that the BOSEM was cycled past its intended operating temperature which could be the case in future operation.
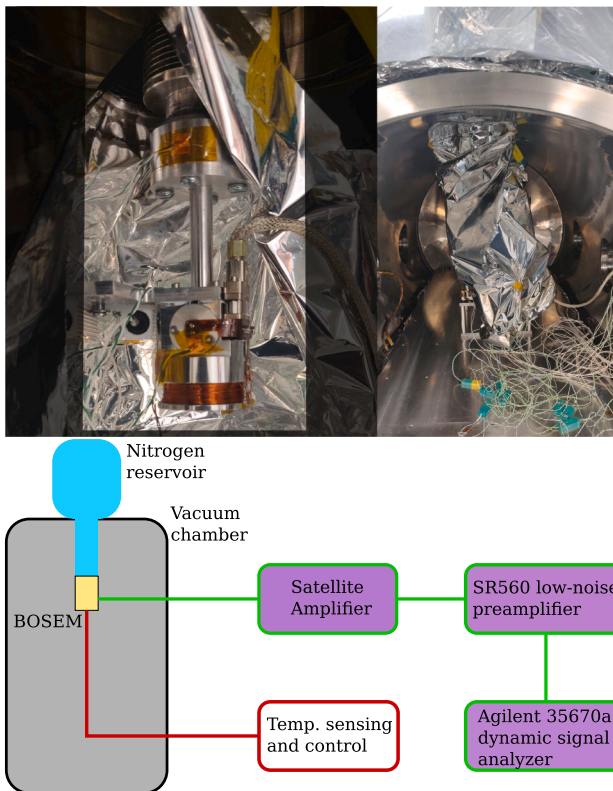

Fig. 5. Temperatures of BOSEM during cool down. the blue curve represents the thermal restrictor plate, and red and yellow were the power resistors. Purple was the side of the BOSEM housing. The PD outer casing is green, and the bottom of the BOSEM is in cyan. The dashed curve shows the maximum temperature of the BOSEM during the simulation where no radiative heating from the vacuum chamber or LED was included.

During the experimental cool down, the temperature differences across the device were not as large as during the simulation, as the top of the thermal restrictor had to also be cooled. This reduced the stresses due to the thermal gradients. It was determined that no significant damage occurred to the BOSEM and its readout scheme after multiple cooling cycles.

3.2. Noise Measurement

In this paper, we tested the shadow sensors without a measured target. Instead, the measurements were taken with the LED either switched on or off, resulting in maximal or zero light from the LED incident on the PD.

The LED drive and PD readout are connected to the satellite amplifier designed for the BOSEMs. The amplifiers signal is usually fed to the LIGOs control and design system for data processing and requires extra whitening of the signal to overcome the noise of the analog-to-digital converters. In our case, the signal was amplified with SR560 low-noise preamplifier [27] and then measured with an AC-coupled Agilent 35670a dynamic signal analyzer [28] with low self-noise.

The shadow sensors have a linear range of $d = 0.7$ mm [25] over which they are nominally operated and is used as an ostensible value to calibrate the devices. The measured displacement corresponds to the changes of the current from the photodetector. This current is then converted to voltage via a satellite amplifier [25] as shown in Fig. 4. The observed voltage is then converted to the displacement using the equation

$$K = \frac{V_{\max}}{d}, \tag{1}$$

where $V_{\max}$ is the maximum voltage on the output of the satellite amplifier. Typical values of the calibration coefficient K are 20–25 kV/m dependent on the parameters of LEDs and photodetectors. In our setup, we measured $K = 20.371$ kV/m.

The response of the device is highly sensitive to temperature, during cool down the PD current increases as shown in Fig. 6. A typical satellite amplifier box contains a 121 kΩ transimpedance amplifier, resulting in the output saturating for a 100 µA PD current input. Projection of the PD current enabled us to predict the correct amplifier gain to use such that the satellite box output does saturate. The transimpedance was reduced to 61.9 kΩ while the calibration factor K increased to 27.635 kV/m at 117.7 K. Noise improvements from cooling occur due to the improved

Fig. 4. Top left: Photo of the BOSEM attached inside the vacuum chamber. Above the BOSEM is the thermal restrictor with power resistors connected. Thermocouples are attached to measure its temperature. **Top right**: Image of the BOSEM setup inside the chamber. The set up is encased in mylar to reduce radiative heating from the tank. **Bottom** The Schematic of the experimental set up labelling the key hardware components.
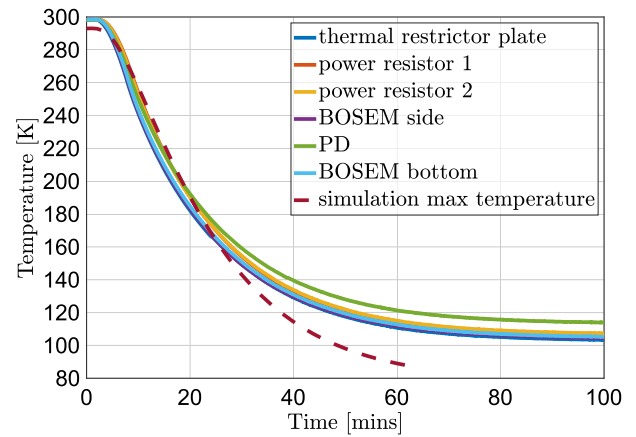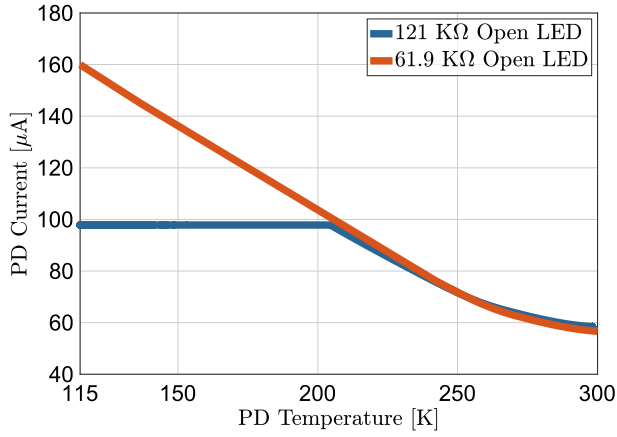
Fig. 6. Comparison of the PD current during cool down. The 61.9 kΩ transimpedance did not cause saturation of the satellite amplifier output unlike the 121 kΩ transimpedance which saturated below 205 K.

quantum efficiency of the LED and photodetector, which results in a stronger signal. Above 10 Hz, the shadow sensors are limited by their photocurrent shot noise spectrum,

$$\sigma_{\text{shot}}^2 = 2eI_{\text{DC}}. \tag{2}$$

where σ_{shot}^2 is the flat white power spectral density of the current, e is the charge of an electron, and I_{DC} is the DC current [29]. We found the shot noise sensitivity at room temperature to be $6 \times 10^{-11} \text{m}/\sqrt{\text{Hz}}$ above 5 Hz as shown in Fig. 7. We note that the value of the shot noise depends on the position on the measured target in the shadow sensor because the I_{DC} changes proportional to the target motion while calibration coefficient K stays the same. During cryogenic operation with the updated transimpedance gain, we observed improvement in the shot noise of the device down to $4.5 \times 10^{-11} \text{m}/\sqrt{\text{Hz}}$ as shown in Fig. 7. The dark noise shown is the photocurrent and electronic noise when no light is incident on the PD, indicating the inherent noise of the readout scheme. The data presented is the result over 100 measurement averages.

3.3. Discussion

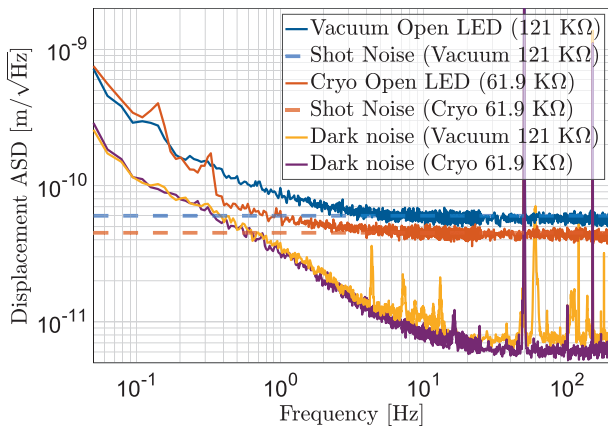The total efficiency of the optical system is defined according to the equation

Fig. 7. Comparisons of the measurements made in vacuum and below 123 K. The high frequency shot noise improvements come from the increased PD current. The measurements contain low frequency peaks which occur due to the temperature stabilisation controller. The 61.9 kΩ transimpenance at room temperature coincided with the blue curve at room temperature.

$$\eta_{\text{tot}} = \eta_{\text{LED}}\eta_{\text{loss}}\eta_{\text{PD}} = \frac{I_{\text{PD}}}{I_{\text{LED}}}, \tag{3}$$

where η_{LED} and η_{PD} are the quantum efficiencies of the LED and photodetector and η_{loss} is the amount of optical power lost between the LED and PD. At room temperature, $\eta_{\text{LED}} \approx 0.058$ and $\eta_{\text{PD}} \approx 0.74$ according to their specifications and $\eta_{\text{tot}} = 60\,\mu\text{A}/35\,\text{mA} = 1.7 \times 10^{-3}$. Therefore, we find $\eta_{\text{loss}} \approx 0.04$. The loss is intentionally introduced by the slit inside the LED carrier (see Fig. 1)) to collimate the beam.

At 117 K, we measure $\eta_{\text{tot}} = 160\,\mu\text{A}/35\,\text{mA} = 4.6 \times 10^{-3}$. Since our finite element modelling shows no significant deformation of the optical system at cryogenic temperatures as discussed in Section 2, we expect that the optical loss η_{loss} is temperature independent. Therefore, the improvement in η_{tot} must come from the photodetector and LED efficiencies. However, since η_{PD} is already 0.75 at room temperature and the LED central wavelength does not significantly change during the cool down (the spectral shift is 0.3 nm/K), we conclude that the photodetector cannot be responsible for the increase of η_{tot} by the observed factor of 2.7.

The LED efficiency can be written as the product of the internal quantum efficiency of gallium arsenide $\eta_{\text{in}} \approx 0.9$ and the external escape efficiency η_{ex}. The escape efficiency is related to the angle of total internal reflection θ between the LED active layer and vacuum [30]. We note that the formalism in [30] neglects the reflection of light on the interface between the LED substrate and its active layer. Therefore, this can be only used as a guidance to understand the cryogenic performance of our LED. As reported in [31], the index of refraction of gallium arsenide reduces at cryogenic temperatures with $dn/dT \approx 10^{-4}\,K^{-1}$ at room temperature. Therefore, we expect that η_{ex} improves due to the increase of the angle of total internal incidences inside the LED. We determined η_{LED} improved to a value of 0.156 when cooled to 117 K.

The majority of the losses of the LED occur due to radiant heat. According to the specifications, up to 98% of the power can be lost as heat at room temperature. It was established that the once cooled to 100 K with a current drive of 35 mA, the power lost to radiant heat was approximately 61 mW corresponding to 84% of the LED's power dissipation.

4. Conclusion

The investigations discussed throughout this paper can be summarised as follows:

- The key conclusion to the results presented in the paper are that the BOSEMs are reliable optical sensors for use at cryogenic temperatures in gravitational wave detectors.
- We simulated and measured BOSEMs at temperatures below 123 K. We found that the currently used satellite amplifiers saturate below 205 K (Fig. 6) due to the enhancement of the LED quantum efficiency at cryogenic temperatures. We have reduced the transimpedance from 121 kΩ down to 61.9 kΩ to avoid the saturation at cryogenic temperatures.
- Maximising the output of the satellite amplifier also improves the shot noise limited sensitivity of the shadow sensors. We achieved the shot noise level of $4.5 \times 10^{-11} \text{m}/\sqrt{\text{Hz}}$ with a fully open photodetector compared to the room temperature sensitivity of $6 \times 10^{-11} \text{m}/\sqrt{\text{Hz}}$ in the same optical configuration. The improvement came from increased LED quantum efficiency from 0.058 at room temperature up to 0.156 at 117 K. The spectrum below 5 Hz was limited by the LED current drive and temperature stabilisation feedback loop which caused peaks in the spectrum (Fig. 7).
- We also found that the first derivative of the PD current over temperature is significantly larger below 200 K compared to the 300 K case. Therefore, temperature fluctuations of BOSEMs should be suppressed in the future gravitational wave detectors for the best

sensing noise of the shadow sensors. The cryogenic system of future gravitational wave detectors should also take into account heating from BOSEM LEDs. Even though the quantum efficiency of the LED improves by a factor of 2.7 at cryogenic temperatures, approximately 84% of power is still radiated as heat around 100 K.

Overall, we conclude that the BOSEMs used for sensing of components within gravitational wave detectors such as LIGO would also be viable sensors for use in cryogenic observatories. Minimal changes would be required to facilitate the process, as only the transimpedance gain of the satellite amplifiers require adjustment to compensate for the improved optical output of the LED. The stresses on the device due to thermocycling do not pose immediate concern to the longevity of these sensors for use at cryogenic temperatures.

Declaration of Competing Interest

The authors declare that they have no known competing financial interests or personal relationships that could have appeared to influence the work reported in this paper.

Acknowledgements

References

[1] Aasi J, Abbott BP, Abbott R, Abbott T, Abernathy MR, Ackley K, Adams C, Adams T, Addesso P, et al. Class Quantum Gravity 2015;32:074001.

[2] Abbott BP, Abbott R, Abbott T, Abernathy M, Acernese F, Ackley K, Adams C, Adams T, Addesso P, Adhikari R, et al. Phys Rev Lett 2016;116:061102.

[3] Abbott BP et al. (LIGO Scientific Collaboration and Virgo Collaboration), Phys Rev X 9, 031040; 2019.

[4] Abbott R et al. (LIGO Scientific Collaboration and Virgo Collaboration), Phys Rev X 11, 021053; 2021.

[5] T.L.S. Collaboration and the Virgo Collaboration, Phys Rev Lett 2016;116: 241103. 10.1103/PhysRevLett.116.241103, arXiv:1606.04855 [gr-qc].

[6] T.L.S. Collaboration, the Virgo Collaboration, et al., Phys. Rev. Lett. 119, 141101 (2017) (2017), 10.1103/PhysRevLett.119.141101, arXiv:1709.09660 [gr-qc].

[7] Abbott R et al. (LIGO Scientific, Virgo), Phys Rev Lett 2020;125: 101102. arXiv: 2009.01075 [gr-qc].

[8] T.L.S. Collaboration and T.V. Collaboration, Phys. Rev. Lett. 119 161101 (2017) (2017), 10.1103/PhysRevLett.119.161101, arXiv:1710.05832 [gr-qc].

[9] Abbott R et al., ApJL 896 L44 896, L44; 2020b.

[10] Martynov DV et al. (LSC Instrument Authors), Phys. Rev. A 95, 043831; 2017.

[11] Buikema A et al. (aLIGO), Phys. Rev. D 102, 062003; 2020. arXiv:2008.01301 [astro-ph.IM].

[12] Somiya K. Class. Quantum Grav 2012;29:124007.

[13] Y. Aso, Y. Michimura, K. Somiya, M. Ando, O. Miyakawa, T. Sekiguchi, D. Tatsumi, and H. Yamamoto (The KAGRA Collaboration), Phys. Rev. D 88, 043007 (2013).

[14] Adhikari RX, et al. Class Quantum Gravity 2020;37:165003.

[15] Maggiore M, et al. J Cosmol Astropart Phys 2020;2020:050.

[16] Abbott BP, et al. Class Quantum Grav 2017;34:044001.

[17] D. Reitze et al., 2019 BAAS 51(7) 035 (2019), arXiv:1907.04833 [astro-ph.IM].

[18] Harry G, Bodiya T, DeSalvo R. Optical Coatings and Thermal Noise in Precision Measurement. Cambridge University Press; 2012.

[19] Gras S, Yu H, Yam W, Martynov D, Evans M. Phys Rev D 2017;95:022001.

[20] Plissi M, Torrie C, Husman M, Robertson N, Strain K, Ward H, Lück H, Hough J. Rev Scient Instrum 2000;71:2539.

[21] T.V.C. (presented Braccini), Classical and Quantum Gravity 19, 1623 (2002).

[22] M. Beker, M. Blom, J. van den Brand, H. Bulten, E. Hennes, and D. Rabeling, Physics Procedia 37, 1389 (2012), proceedings of the 2nd International Conference on Technology and Instrumentation in Particle Physics (TIPP 2011).

[23] Strain KA, Shapiro BN. Rev Sci Instrum 2012;83:044501.

[24] Akutsu T, Arellano FEP, Shoda A, Fujii Y, Okutomi K, Barton MA, Takahashi R, Komori K, Aritomi N, Shimoda T, Takano S, Takeda H, Martin ENTS, Kozu R, Ikenoue B, Obuchi Y, Fukushima M, Aso Y, Michimura Y, Miyakawa O, Kamiizumi M. Rev Sci Instrum 2020;91:115001.

[25] Carbone L, et al. Class Quant Grav 2012;29:115005. arXiv:1205.5643 [gr-qc].

[26] Autodesk, "Autodesk empowers innovators everywhere to make the new possible, (2021).

[27] S.R. Systems, "Srs sr560 low-noise preamplifier, (2021).

[28] K. Technologies, "35670a dynamic signal analyzer, (2017).

[29] Bramsiepe SG, Loomes D, Middlemiss RP, Paul DJ, Hammond GD. IEEE Sens J 2018;18:4108.

[30] R. Hui, in Introduction to Fiber-Optic Communications, edited by R. Hui (Academic Press, 2020) pp. 77–124.

[31] McCaulley JA, Donnelly VM, Vernon M, Taha I. Phys Rev B 1994;49:7408.